Structural basis of INTAC-regulated transcription

Hai Zheng[1*], Qianwei Jin[1*], Yilun Qi[1], Weida Liu[1], Yulei Ren[1], Xinxin Wang[1], Fei Chen[1], Jingdong Cheng[1], Xizi Chen[1], and Yanhui Xu[1,2,3]†

[1]Fudan University Shanghai Cancer Center, Institutes of Biomedical Sciences, State Key Laboratory of Genetic Engineering, Shanghai Key Laboratory of Radiation Oncology, and Shanghai Key Laboratory of Medical Epigenetics, Shanghai Medical College of Fudan University, Shanghai 200032, China.

[2]The International Co-laboratory of Medical Epigenetics and Metabolism, Ministry of Science and Technology, China, Department of Systems Biology for Medicine, School of Basic Medical Sciences, Shanghai Medical College of Fudan University, Shanghai 200032, China.

[3]Human Phenome Institute, Collaborative Innovation Center of Genetics and Development, School of Life Sciences, Fudan University, Shanghai 200433, China

* These authors contributed equally to this work.
† To whom correspondence should be addressed. E-mail: xuyh@fudan.edu.cn

18   **Abstract**

19   For the majority of expressed eukaryotic genes, RNA polymerase II (Pol II) forms a paused

20   elongation complex (PEC) and undergoes promoter-proximal pausing downstream of the

21   transcription start site [1-3]. The polymerase either proceeds into productive elongation or

22   undergoes promoter-proximal premature transcription termination [4-6]. It remains incompletely

23   understood how transcription is regulated at this stage. Here, we determined the structure of

24   PEC bound to INTAC, an Integrator-containing PP2A complex [7], at near-atomic resolution. The

25   structure shows that INTAC partially wraps around PEC through multiple contacts, permitting

26   the memetic nascent RNA to run into substrate-entry tunnel of the endonuclease subunit

27   INTS11 of INTAC for cleavage. Pol II C-terminal domain (CTD) winds over INTAC backbone

28   module through multiple anchors and is suspended above the phosphatase of INTAC for

29   dephosphorylation. Biochemical analysis shows that INTAC-PEC association requires

30   unphosphorylated CTD and could tolerate CTD phosphorylation, suggesting an INTAC-

31   mediated persistent CTD dephosphorylation followed by reinforcement of the INTAC-PEC

32   complex. Our study reveals how INTAC binds PEC and orchestrates RNA cleavage and CTD

33   dephosphorylation, two critical events in generating premature transcription termination.

Introduction

Eukaryotic transcription by RNA polymerase II (Pol II) is a strictly regulated process that involves the interplay of numerous factors [4,5]. Promoter-proximal pausing is a regulatory mechanism that connects transcription initiation and productive elongation in metazoan [3,6]. It typically occurs at 20–200 base pairs downstream of the transcription start site (TSS) and can be observed at the majority of expressed genes [1,2]. Pol II forms a paused elongation complex (PEC) through binding of two factors: the 5,6-dichloro-1-β-d-ribofuranosylbenzimidazole (DRB) sensitivity-inducing factor (DSIF), consisting of subunits SPT4 and SPT5, and the negative elongation factor (NELF), consisting of the four subunits NELF-A, -B, -C/D and -E [8-11]. Following the duration of pausing, the polymerase either proceeds into productive elongation or undergoes promoter-proximal premature transcription termination (PTT) [12], which plays a decisive role in determining transcriptional outputs. Nonetheless, it remains unclear how the fate of PEC is governed mechanistically.

In contrast to the well-characterized pause release and productive elongation [4,5], the mechanism of PTT remains largely unknown. Emerging evidence implies that metazoan-specific Integrator complex involves this process. Integrator complex [13,14] functions as an RNA endonuclease to cleave different classes of RNAs [15-19]. More recent studies discovered that Integrator is enriched in the proximity of RNA promoters [20] and can associate with paused Pol II bound by DSIF and NELF [21,22] to trigger PTT and repress gene activity [18,23-28]. We have recently found that Integrator associates with protein phosphatase 2A core enzyme (PP2A-AC) and dephosphorylates the C-terminal domain (CTD) of Pol II and determined the structure of Integrator-containing PP2A-AC (termed INTAC), showing how the RNA nuclease and protein phosphatase are organized in the INTAC complex [7]. In addition, Integrator-bound PP2A dephosphorylates Pol II CTD and Spt5 to prevent the transition to productive elongation [7,24,29]. Despite these studies, it remains elusive how INTAC, especially its two catalytic modules, is structurally organized and functionally coordinated in the context of PEC and how INTAC works with PEC in PTT.

Structure determination of INTAC-PEC complex

To investigate the mechanistic implications of INTAC in promoter-proximal pausing, we purified the human INTAC [7], NELF, DSIF, and pig (S. scrofa) Pol II, which has 99.9% sequence identity to human Pol II except for four amino acids (Extended Data Fig. 1, a, b). The INTAC-PEC complex was assembled by adding INTAC, NELF, and DSIF to an elongation complex that was pre-assembled by mixing Pol II and a DNA-RNA hybrid [30,31] (Methods). The assembled INTAC-PEC complex was subjected to gradient fixation (GraFix), followed by cryo-electron microscopy (cryo-EM) single particle reconstruction (Extended Data Fig. 2). The cryo-

70 EM map was refined to 4.5 Å resolution and the maps of subcomplexes were improved to near-
71 atomic (3.8 Å to 4.1 Å) resolution by focused refinement. Structural model was built by fitting
72 previously determined structures of INTAC [7] and PEC [30] into the cryo-EM maps followed by
73 manual adjustment (Extended Data Fig. 3, Extended Data Table 1).

74

Overall structure of INTAC-PEC complex

76 The INTAC-PEC complex structure reveals a compact fold with approximate dimensions
77 of ~280× 270× 260 Å^3 (Fig. 1, Extended Data Fig. 4, Supplementary Video 1). As observed in
78 the apo PEC structure [30], NELF and DSIF wrap around the central Pol II, generating a compact
79 globular fold. The PEC complex sits above the main body of INTAC through interface-I/-II/-V
80 and is further stabilized by two INTAC protrusions on opposite sides at interface-III/-IV,
81 resembling a ball (PEC) in a bucket (INTAC). Consistent with the modular organization of the
82 apo INTAC complex [7], the shoulder and backbone modules of INTAC within INTAC-PEC
83 generate a central cruciform scaffold with the phosphatase and endonuclease modules flanking
84 the opposite sides. A previously undetected tail module extends out of the bottom of the
85 backbone module and folds back to bind Pol II. Three putative Pol II CTD fragments wind on
86 the surface of INTAC backbone module and an additional fragments is suspended above the
87 catalytic pocket of the phosphatase subunit PP2A-C, indicative of a path favorable for INTAC-
88 mediated CTD association and dephosphorylation (Supplementary Video 2).

89 The DNA duplex is opened in the catalytic cavity with the template strand forming a one-
90 turn DNA-RNA hybrid, and reanneals into a duplex that protrudes out of Pol II through the exit
91 tunnel (Fig. 1b, Extended Data Fig. 4). Both exit and entry DNAs point away from INTAC,
92 suggesting that INTAC generates no clash with DNA and that INTAC does not directly affect
93 transcription elongation. The memetic nascent RNA runs out through the RNA exit tunnel of
94 Pol II, is brought into proximity of INTAC by Pol II-SPT5-INTS11 interactions at interface-V,
95 and runs into the RNA entry tunnel of the endonuclease subunit INTS11. The last visible RNA
96 nucleotide is suspended above the active site of INTS11. The structure reveals INTAC-PEC
97 organization that favors RNA cleavage and Pol II CTD dephosphorylation.

98

The interfaces between INTAC and Pol II-NELF

100 INTAC makes three direct contacts with Pol II (Fig. 2, a to d, Extended Data Fig. 5). At
101 the interface-I, the C-terminal α-helix of RPB11 contacts the helical repeat 1 of INTS2
102 (INTS2^{HR1}). At the interface-II, the C-terminal helix of INTS7 binds the domain2 of RPB3 and
103 the C-terminal end of INTS4 bridges the contact between INTS9 and the zinc loop of RPB3.
104 The N-terminal HEAT (huntingtin, elongation factor 3, protein phosphatase 2A and TOR1)

105   domain of INTS1 adopts an arch-shaped fold and forms the tail module, which caps the exposed

106   end of the scaffold module and flanks away from the core INTAC. The two RPB2 external

107   domains of Pol II contact the tail on the convex ridge at the interface-III. This tail module was

108   not observed in the apo INTAC structure (Extended Data Fig. 4a), suggesting a PEC-mediated

109   tail stabilization and a potential function of tail in recruitment of PEC.

110   INTS6 bridges the phosphatase of INTAC and the NELF-B-NELF-E lobe [30] of PEC (Fig.

111   2, a, e, Extended Data Fig. 5). At the interface-IV, the exposed end of the INTS6 β-barrel domain

112   contacts the HEAT domain of NELF-B, consistent with known interaction between Integrator

113   and NELF [21,22]. In addition, INTS6 [7] and NELF-B [30] are highly conserved in primary sequence

114   among vertebrates, suggesting a conserved contact across species. At the interface-V, the SPT5

115   KOWx-4 domain packs on Pol II, stabilizes the exit RNA, and contacts the INTS11 (Fig. 2, a,

116   f). As discussed below, the interaction brings RNA to INTS11 for cleavage.

117

The Pol II CTD-INTAC interface

119   The human Pol II CTD consists of 52 consensus heptapeptide repeats (Tyr1-Ser2-Pro3-

120   Thr4-Ser5-Pro6-Ser7) and the phosphorylation levels at Ser2, Ser5, and Ser7 change

121   dynamically throughout the transcription cycle, exhibiting distinct patterns for initiation,

122   elongation, and termination [32]. Cryo-EM map reveals four putative Pol II CTD segments,

123   indicative of a potential CTD-binding path toward the active center of PP2A-C for

124   dephosphorylation (Fig. 3a, Extended Data Fig. 6, Supplementary Video 2). Pol II and INTAC

125   generate a center-hollowed cradle with the CTD-binding path of INTAC being ~50 Å away

126   from the last modeled RPB1 residue (P1487). This cradle may accommodate Pol II CTD repeats

127   above the three CTD anchoring sites.

128   The CTD-1 to CTD-3 segments span ~50 Å and are sequentially arrayed on the surface of

129   INTAC backbone (Fig. 3a, Extended Data Fig. 6, Supplementary Video 2). The CTD-1 (~5

130   residues) packs against a relatively hydrophobic pocket of the HEAT repeat of INTS4. The

131   CTD-2 (~13 residues) forms a U-turn coil and packs against the molecular junction of INTS2,

132   INTS4, and INTS7 and is stabilized by a network on interactions. Particularly, two tyrosine (Y^1)

133   residues anchor on the surface of INTS7 HEAT repeat and sandwich residue R73 of INTS7,

134   generating stacking interaction. The CTD-3 (~8 residues) anchors into a hydrophobic pocket

135   formed by INTS2 and an extending loop of INTS6.

136   Relatively weak cryo-EM map was observed above the catalytic pocket of PP2A-C (Fig.

137   3a, Extended Data Fig. 6, c, g). The density is likely derived from Pol II CTD or the N-terminal

138   tail of INTS6 and was termed CTD-4 for simplicity. This U-shaped fragment (~7 residues) is

139   positioned within the substrate-binding groove of PP2A-C. Three central residues are

140   suspended above the catalytic center, in a manner similar to microcystin LR (MCLR, PP2A

141   inhibitor) in the PP2A holoenzyme structure [33]. The Cα atom of the central residue is ~7 Å away

142   from the near catalytic manganese cation, suggesting a position of phosphorylated Ser5 residue

143   of CTD for dephosphorylation. CTD-4 is ~50 Å away from CTD-3, indicative of a putative

144   CTD path of ~100 Å in length from Pol II body (P1487) to CTD-3 and then to PP2A-C active

145   site.

146

Pol II CTD is required for INTAC-PEC interaction

148   To further investigate how INTAC-PEC complex is assembled, we performed in vitro

149   pulldown assay using immobilized INTAC and individually purified NELF, DSIF (Fig. 3b,

150   Extended Data Fig. 1, c, d). We also overexpressed and purified human Pol II (hPol II) and a

151   CTD-truncated hPol II (hPol II$^{\Delta CTD}$) in Expi293F cells (Extended Data Fig. 1a). Consistent with

152   previous studies [7,19], INTAC could pull out hPol II with nearly 1:1 stoichiometry (Fig. 3b, lanes

153   13-14). In contrast, the deletion of CTD impaired INTAC-hPol II interaction (lane 15) and

154   isolated CTD could pull out INTAC (Extended Data Fig. 1c). The immobilized DSIF or NELF

155   exhibited a weak but detectable binding with INTAC (Extended Data Fig. 1d), consistent with

156   previous studies showing their binding to Integrator independent of DNA/RNA [21,22]. In

157   agreement with this weak interaction and their limited contact with INTAC (Fig. 2), the addition

158   of DSIF and NELF showed nearly undetectable effect on Pol II-INTAC interaction (Fig. 3b,

159   lanes 15, 17). Interestingly, the addition of a DNA-RNA bubble to hPol II$^{\Delta CTD}$, along with DSIF

160   and NELF, caused a slight increase in binding to INTAC (lanes 17, 19), suggesting that the

161   exiting RNA may facilitate the binding of PEC to INTAC. The above result underscores the

162   critical role of CTD in the recruitment of INTAC to Pol II and the assembly of INTAC-PEC.

163   NELF, DSIF, and nascent RNA may together facilitate organizing the complex and allow

164   efficient CTD dephosphorylation and RNA cleavage.

165   The in vitro pulldown assay further showed that INTAC binds and dephosphorylates

166   phosphorylated Pol II (Fig. 3c, lanes 9-10). The addition of PP2A inhibitor hampered the

167   dephosphorylation and binding of Pol II to INTAC (lane 11), as compared to the

168   unphosphorylated Pol II (lanes, 10, 12, 13). The result suggests that CTD phosphorylation

169   partially inhibits INTAC-Pol II interaction and INTAC may tolerate CTD phosphorylation to

170   some extent.

171   In the presence of NELF and DSIF, INTAC showed a comparable binding to

172   phosphorylated and unphosphorylated Pol II (Fig. 3c, lanes 18-22). NELF and DSIF enhanced

173   INTAC-Pol II interaction and the dephosphorylated CTD may reinforce INTAC-CTD

174   interaction. Structural and biochemical analyses together lead to a model of CTD

175   dephosphorylation. Upon formation of INTAC-PEC complex, un/dephosphorylated CTD

176   occupies the CTD-binding sites of INTAC and evicts, if any, the bound phosphorylated CTD,

177　which is further brought to PP2A-C for dephosphorylation. Thus, INTAC ensures a persistent

178　and complete CTD dephosphorylation for early termination.

179

INTS11 is activated upon INTAC-PEC assembly

181　　　Consistent with previous studies [30,31], the INTAC-PEC structure shows that SPT5 and

182　SPT4, the two DSIF subunits, bind Pol II around stalk, clamp, and wall, with multiple domains

183　surrounding the entry DNA and exit RNA (Figs. 1, 4a, Extended Data Fig. 7, Supplementary

184　Video 3). The SPT5 KOWx-4 and KOW5 domains function as an "RNA clamp" and contact

185　INTAC on INTS9-INTS11 heterodimer. At the interface-V, the INTS11 metallo-β-lactamase

186　domain binds the SPT5 KOWx-4 domain, which bridges the RNA exit tunnel of Pol II and

187　RNA entry tunnel of INTS11. Although DSIF, NELF, and Pol II body are not essentially

188　required for binding to INTAC, INTAC-PEC interactions at interface-I to -V may maintain the

189　overall modular organization and guide RNA to the active center of INTS11 for cleavage.

190　　　INTS11 exhibits a closed, inactive conformation in the structures of RNA-free INTAC [7]

191　and the isolated endonuclease module (INTS4-INTS9-INTS11) [34] (Fig. 4a, Extended Data Fig.

192　7, Supplementary Video 4). Superposition of INTS11 metallo-β-lactamase domain shows that

193　the association of RNA-bound PEC induces a rotation of INTS11 β-CASP domain by ~15

194　degrees and an opening of the substrate-binding tunnel by ~5 Å, permitting the entry of the

195　RNA for cleavage. Structural comparison suggests an activation of INTS11 upon assembly of

196　INTAC-PEC.

197

RNA is brought to INTS11 for cleavage

199　　　Among the 23 RNA nucleotides used in structure determination, nucleotides -1 to -10

200　(relative to the NTP addition site) form DNA-RNA hybrid within Pol II and the following strand

201　(-10 to -16) winds out of RNA exit tunnel (Fig. 4, b, c, Extended Data Fig. 7). A weak but

202　noticeable cryo-EM map showed a linker RNA (-16 to -18), consistent with its lack of protein

203　contact. The four preceding nucleotides (-18 to -21) insert into the RNA entry tunnel of INTS11

204　with the phosphate and ribose groups well-ordered. The phosphate groups face downward the

205　RNA entry tunnel while the bases face outward and are sandwiched by hydrophobic cleft,

206　consistent with non-RNA sequence specificity of INTS11 (Fig. 4d, Supplementary Video 3).

207　　　Nucleotide U^{-21} is suspended near the active site of INTS11 and its phosphate group and

208　the two preceding nucleotides (-22 and -23) were nearly invisible, indicative of a position of

209　RNA cleavage, ~20 nucleotides upstream of the NTP addition site (Fig. 4, c to e, Extended Data

210　Fig. 7b). If the RNA were not cleaved, the phosphate group of U^{-21} would be stabilized by

211　residue H392 of INTS11 with the two phosphate oxygen atoms being ~3 Å away from the two

212   catalytic zinc cations. The preceding nucleotide would be stabilized by residue Y353 of INTS11.
213   The organization of catalytic pocket and the placement of RNA substrate are generally similar
214   to that of cleavage and polyadenylation specificity factor (CPSF) CPSF73 in the histone pre-
215   mRNA cleavage complex (HCC) complex (Extended Data Fig. 7c), which adopts an active
216   state, poised for the cleavage reaction [35].

217   It has been reported that the nucleic acid binding module INTS10-INTS13-INTS14 of
218   INTAC preferentially binds RNA stem loop regions and brings the endonuclease module to
219   target transcripts for cleavage [36]. This subcomplex was not observed in our structure, possibly
220   due to the lack of stabilization by exposed/uncleaved RNA.

221

INTAC generates steric clash with PAF1C and SPT6 of the EC* complex

223   INTAC has been demonstrated to be involved in NELF- and DSIF-dependent promoter-
224   proximal pausing [21,22,28]. Recent studies have shown that PAF1 complex (PAF1C) regulates the
225   stabilization of pausing in addition to its role in promoting elongation [37]. An activated
226   transcription elongation complex EC* is formed by Pol II, PAF1C, DSIF, and SPT6 [31].
227   Comparison of the INTAC-PEC structure and the EC* structure shows that the PAF1C subunits
228   PAF1 and LEO1 generate steric hindrance with the tail module of INTAC and CTR9 has clash
229   with INTS2^{HR1} of INTAC [7] (Extended Data Fig. 4c). In addition, the SPT6 core around the exit
230   RNA clashes with INTS11 and the SPT6 tSH2 domain has clashes with the INTS6 vWA domain.
231   The above structural comparison shows that PAF1C and INTAC may form independent
232   complexes with paused Pol II, or conformational changes of PAF1C or INTAC are required for
233   their co-existence with a Pol II.

234

INTAC works with PEC to orchestrate CTD dephosphorylation and RNA cleavage for premature transcription termination

237   Mounting evidence has shown that Integrator's function in snRNA cleavage is rather an
238   exception and that INTAC confers more profound role in transcription regulation. Our study
239   reveals the molecular mechanism by which INTAC shapes the organization of paused Pol II
240   and induces premature transcription termination via the cleavage of nascent RNA by its
241   endonuclease module and the dephosphorylation of Pol II CTD by its phosphatase module.
242   Recruitment of the endonuclease module to nascent RNA requires binding of Pol II CTD to
243   INTAC, which prefers un/dephosphorylated CTD and could tolerate CTD phosphorylation,
244   especially in the presence of NELF and DSIF. The paused Pol II and the cleavage of nascent
245   RNA are thought to destabilize Pol II and lead to exonuclease Xrn2-mediated termination of
246   transcription [38]. The structure also provides a framework for further study of Integrator's

8

247   functions in transcription termination of coding genes and processing of non-coding RNAs [16-
248   19,26,27].

249   During manuscript preparation, Fianu et. al. reported cryo-EM structure of Intergrator-
250   PP2A bound to PEC [39]. The structure is generally similar to our structure except that RNA was
251   not observed in the RNA entry tunnel of INTS11. Moreover, only one CTD fragment (CTD-2
252   in our study) was observed, possibly because the Intergrator-PP2A was assembled by mixing
253   three subcomplexes. Nevertheless, our independent study confirms the molecular mechanism
254   of INTAC-PEC assembly and provides additional insights into RNA cleavage by INTS11 and
255   INTAC-mediated Pol II CTD recognition and dephosphorylation.

Reference:

1   Jonkers, I., Kwak, H. & Lis, J. T. Genome-wide dynamics of Pol II elongation and its interplay with promoter proximal pausing, chromatin, and exons. *Elife* **3**, e02407, doi:10.7554/eLife.02407 (2014).

2   Day, D. S. *et al.* Comprehensive analysis of promoter-proximal RNA polymerase II pausing across mammalian cell types. *Genome Biol* **17**, 120, doi:10.1186/s13059-016-0984-2 (2016).

3   Core, L. & Adelman, K. Promoter-proximal pausing of RNA polymerase II: a nexus of gene regulation. *Genes Dev* **33**, 960-982, doi:10.1101/gad.325142.119 (2019).

4   Jonkers, I. & Lis, J. T. Getting up to speed with transcription elongation by RNA polymerase II. *Nat Rev Mol Cell Biol* **16**, 167-177, doi:10.1038/nrm3953 (2015).

5   Chen, F. X., Smith, E. R. & Shilatifard, A. Born to run: control of transcription elongation by RNA polymerase II. *Nat Rev Mol Cell Biol* **19**, 464-478, doi:10.1038/s41580-018-0010-5 (2018).

6   Kamieniarz-Gdula, K. & Proudfoot, N. J. Transcriptional Control by Premature Termination: A Forgotten Mechanism. *Trends Genet* **35**, 553-564, doi:10.1016/j.tig.2019.05.005 (2019).

7   Zheng, H. *et al.* Identification of Integrator-PP2A complex (INTAC), an RNA polymerase II phosphatase. *Science* **370**, eabb5872, doi:10.1126/science.abb5872 (2020).

8   Wu, C. H. *et al.* NELF and DSIF cause promoter proximal pausing on the hsp70 promoter in Drosophila. *Genes Dev* **17**, 1402-1414, doi:10.1101/gad.1091403 (2003).

9   Missra, A. & Gilmour, D. S. Interactions between DSIF (DRB sensitivity inducing factor), NELF (negative elongation factor), and the Drosophila RNA polymerase II transcription elongation complex. *Proc Natl Acad Sci U S A* **107**, 11301-11306, doi:10.1073/pnas.1000681107 (2010).

10   Wada, T. *et al.* DSIF, a novel transcription elongation factor that regulates RNA polymerase II processivity, is composed of human Spt4 and Spt5 homologs. *Genes Dev* **12**, 343-356, doi:10.1101/gad.12.3.343 (1998).

11   Yamaguchi, Y. *et al.* NELF, a multisubunit complex containing RD, cooperates with DSIF to repress RNA polymerase II elongation. *Cell* **97**, 41-51, doi:10.1016/s0092-8674(00)80713-8 (1999).

12   Evans, R., Weber, J., Ziff, E. & Darnell, J. E. Premature termination during adenovirus transcription. *Nature* **278**, 367-370, doi:10.1038/278367a0 (1979).

13   Mendoza-Figueroa, M. S., Tatomer, D. C. & Wilusz, J. E. The Integrator Complex in Transcription and Development. *Trends Biochem Sci* **45**, 923-934, doi:10.1016/j.tibs.2020.07.004 (2020).

14   Baillat, D. & Wagner, E. J. Integrator: surprisingly diverse functions in gene expression. *Trends Biochem Sci* **40**, 257-264, doi:10.1016/j.tibs.2015.03.005 (2015).

15   Cazalla, D., Xie, M. & Steitz, J. A. A primate herpesvirus uses the integrator complex to generate viral microRNAs. *Mol Cell* **43**, 982-992, doi:10.1016/j.molcel.2011.07.025 (2011).

298 16 Xie, M. *et al.* The host Integrator complex acts in transcription-independent maturation
299   of herpesvirus microRNA 3' ends. *Genes Dev* **29**, 1552-1564,
300   doi:10.1101/gad.266973.115 (2015).
301 17 Lai, F., Gardini, A., Zhang, A. & Shiekhattar, R. Integrator mediates the biogenesis of
302   enhancer RNAs. *Nature* **525**, 399-403, doi:10.1038/nature14906 (2015).
303 18 Skaar, J. R. *et al.* The Integrator complex controls the termination of transcription at
304   diverse classes of gene targets. *Cell Res* **25**, 288-305, doi:10.1038/cr.2015.19 (2015).
305 19 Baillat, D. *et al.* Integrator, a multiprotein mediator of small nuclear RNA processing,
306   associates with the C-terminal repeat of RNA polymerase II. *Cell* **123**, 265-276,
307   doi:10.1016/j.cell.2005.08.019 (2005).
308 20 Gardini, A. *et al.* Integrator regulates transcriptional initiation and pause release
309   following activation. *Mol Cell* **56**, 128-139, doi:10.1016/j.molcel.2014.08.004 (2014).
310 21 Yamamoto, J. *et al.* DSIF and NELF interact with Integrator to specify the correct post-
311   transcriptional fate of snRNA genes. *Nat Commun* **5**, 4263, doi:10.1038/ncomms5263
312   (2014).
313 22 Stadelmayer, B. *et al.* Integrator complex regulates NELF-mediated RNA polymerase
314   II pause/release and processivity at coding genes. *Nat Commun* **5**, 5531,
315   doi:10.1038/ncomms6531 (2014).
316 23 Lykke-Andersen, S. *et al.* Integrator is a genome-wide attenuator of non-productive
317   transcription. *Mol Cell* **81**, 514-529 e516, doi:10.1016/j.molcel.2020.12.014 (2021).
318 24 Huang, K. L. *et al.* Integrator Recruits Protein Phosphatase 2A to Prevent Pause Release
319   and Facilitate Transcription Termination. *Mol Cell* **80**, 345-358 e349,
320   doi:10.1016/j.molcel.2020.08.016 (2020).
321 25 Beckedorff, F. *et al.* The Human Integrator Complex Facilitates Transcriptional
322   Elongation by Endonucleolytic Cleavage of Nascent Transcripts. *Cell Rep* **32**, 107917,
323   doi:10.1016/j.celrep.2020.107917 (2020).
324 26 Tatomer, D. C. *et al.* The Integrator complex cleaves nascent mRNAs to attenuate
325   transcription. *Genes Dev* **33**, 1525-1538, doi:10.1101/gad.330167.119 (2019).
326 27 Rubtsova, M. P. *et al.* Integrator is a key component of human telomerase RNA
327   biogenesis. *Sci Rep* **9**, 1701, doi:10.1038/s41598-018-38297-6 (2019).
328 28 Elrod, N. D. *et al.* The Integrator Complex Attenuates Promoter-Proximal Transcription
329   at Protein-Coding Genes. *Mol Cell* **76**, 738-752 e737,
330   doi:10.1016/j.molcel.2019.10.034 (2019).
331 29 Vervoort, S. J. *et al.* The PP2A-Integrator-CDK9 axis fine-tunes transcription and can
332   be targeted therapeutically in cancer. *Cell* **184**, 3143-3162 e3132,
333   doi:10.1016/j.cell.2021.04.022 (2021).
334 30 Vos, S. M., Farnung, L., Urlaub, H. & Cramer, P. Structure of paused transcription
335   complex Pol II-DSIF-NELF. *Nature* **560**, 601-606, doi:10.1038/s41586-018-0442-2
336   (2018).
337 31 Vos, S. M. *et al.* Structure of activated transcription complex Pol II-DSIF-PAF-SPT6.
338   *Nature* **560**, 607-612, doi:10.1038/s41586-018-0440-4 (2018).
339 32 Harlen, K. M. & Churchman, L. S. The code and beyond: transcription regulation by

340   the RNA polymerase II carboxy-terminal domain. *Nat Rev Mol Cell Biol* **18**, 263-273,
341   doi:10.1038/nrm.2017.10 (2017).

342 33 Xu, Y. *et al.* Structure of the protein phosphatase 2A holoenzyme. *Cell* **127**, 1239-1251,
343   doi:10.1016/j.cell.2006.11.033 (2006).

344 34 Pfleiderer, M. M. & Galej, W. P. Structure of the catalytic core of the Integrator complex.
345   *Mol Cell* **81**, 1246-1259 e1248, doi:10.1016/j.molcel.2021.01.005 (2021).

346 35 Sun, Y. *et al.* Structure of an active human histone pre-mRNA 3'-end processing
347   machinery. *Science* **367**, 700-703, doi:10.1126/science.aaz7758 (2020).

348 36 Sabath, K. *et al.* INTS10-INTS13-INTS14 form a functional module of Integrator that
349   binds nucleic acids and the cleavage module. *Nat Commun* **11**, 3422,
350   doi:10.1038/s41467-020-17232-2 (2020).

351 37 Chen, F. X. *et al.* PAF1, a Molecular Regulator of Promoter-Proximal Pausing by RNA
352   Polymerase II. *Cell* **162**, 1003-1015, doi:10.1016/j.cell.2015.07.042 (2015).

353 38 Proudfoot, N. J. Transcriptional termination in mammals: Stopping the RNA
354   polymerase II juggernaut. *Science* **352**, aad9926, doi:10.1126/science.aad9926 (2016).

355 39 Fianu, I. *et al.* Structural basis of Integrator-mediated transcription regulation. *Science*
356   **374**, 883-887, doi:10.1126/science.abk0154 (2021).

357 40 Chen, X. *et al.* Structures of the human Mediator and Mediator-bound preinitiation
358   complex. *Science* **372**, eabg0635, doi:10.1126/science.abg0635 (2021).

359 41 Chen, X. *et al.* Structural insights into preinitiation complex assembly on core
360   promoters. *Science* **372**, eaba8490, doi:10.1126/science.aba8490 (2021).

361 42 Kastner, B. *et al.* GraFix: sample preparation for single-particle electron
362   cryomicroscopy. *Nat Methods* **5**, 53-55, doi:10.1038/nmeth1139 (2008).

363 43 Mastronarde, D. N. Automated electron microscope tomography using robust prediction
364   of specimen movements. *J Struct Biol* **152**, 36-51, doi:10.1016/j.jsb.2005.07.007 (2005).

365 44 Zheng, S. Q. *et al.* MotionCor2: anisotropic correction of beam-induced motion for
366   improved cryo-electron microscopy. *Nat Methods* **14**, 331-332,
367   doi:10.1038/nmeth.4193 (2017).

368 45 Scheres, S. H. RELION: implementation of a Bayesian approach to cryo-EM structure
369   determination. *J Struct Biol* **180**, 519-530, doi:10.1016/j.jsb.2012.09.006 (2012).

370 46 Punjani, A., Rubinstein, J. L., Fleet, D. J. & Brubaker, M. A. cryoSPARC: algorithms
371   for rapid unsupervised cryo-EM structure determination. *Nat Methods* **14**, 290-296,
372   doi:10.1038/nmeth.4169 (2017).

373 47 Pettersen, E. F. *et al.* UCSF Chimera--a visualization system for exploratory research
374   and analysis. *J Comput Chem* **25**, 1605-1612, doi:10.1002/jcc.20084 (2004).

375 48 Pettersen, E. F. *et al.* UCSF ChimeraX: Structure visualization for researchers,
376   educators, and developers. *Protein Sci* **30**, 70-82, doi:10.1002/pro.3943 (2021).

377 49 Emsley, P. & Cowtan, K. Coot: model-building tools for molecular graphics. *Acta*
378   *Crystallogr D Biol Crystallogr* **60**, 2126-2132, doi:10.1107/S0907444904019158
379   (2004).

380 50 Jumper, J. *et al.* Highly accurate protein structure prediction with AlphaFold. *Nature*
381   **596**, 583-589, doi:10.1038/s41586-021-03819-2 (2021).

382   51   Adams, P. D. *et al.* PHENIX: building new software for automated crystallographic
383   structure determination. *Acta Crystallogr D Biol Crystallogr* **58**, 1948-1954,
384   doi:10.1107/s0907444902016657 (2002).
385   52   Chen, V. B. *et al.* MolProbity: all-atom structure validation for macromolecular
386   crystallography. *Acta   Crystallogr   D   Biol   Crystallogr*   **66**,   12-21,
387   doi:10.1107/S0907444909042073 (2010).
388   53   Barad, B. A. *et al.* EMRinger: side chain–directed model and map validation for 3D
389   cryo-electron microscopy. *Nature Methods* **12**, 943-946, doi:10.1038/nmeth.3541
390   (2015).
391

400   **Author contributions**: H. Z. prepared the samples for structural and biochemical analyses with
401   help from F. C., X. W., and X. C; Q. J. collected the data and performed EM analyses and model
402   building with help from Y. Q., W. L., Y. R. and J. C.; Y. X. and H. Z. wrote the manuscript; Y.
403   X. supervised the project.

404   **Competing interests**: Authors declare no competing interests.

405   **Data and materials availability**: Cryo-EM maps and atomic coordinates will be deposited in
406   the EMDB and PDB upon the acceptance of this manuscript.

14
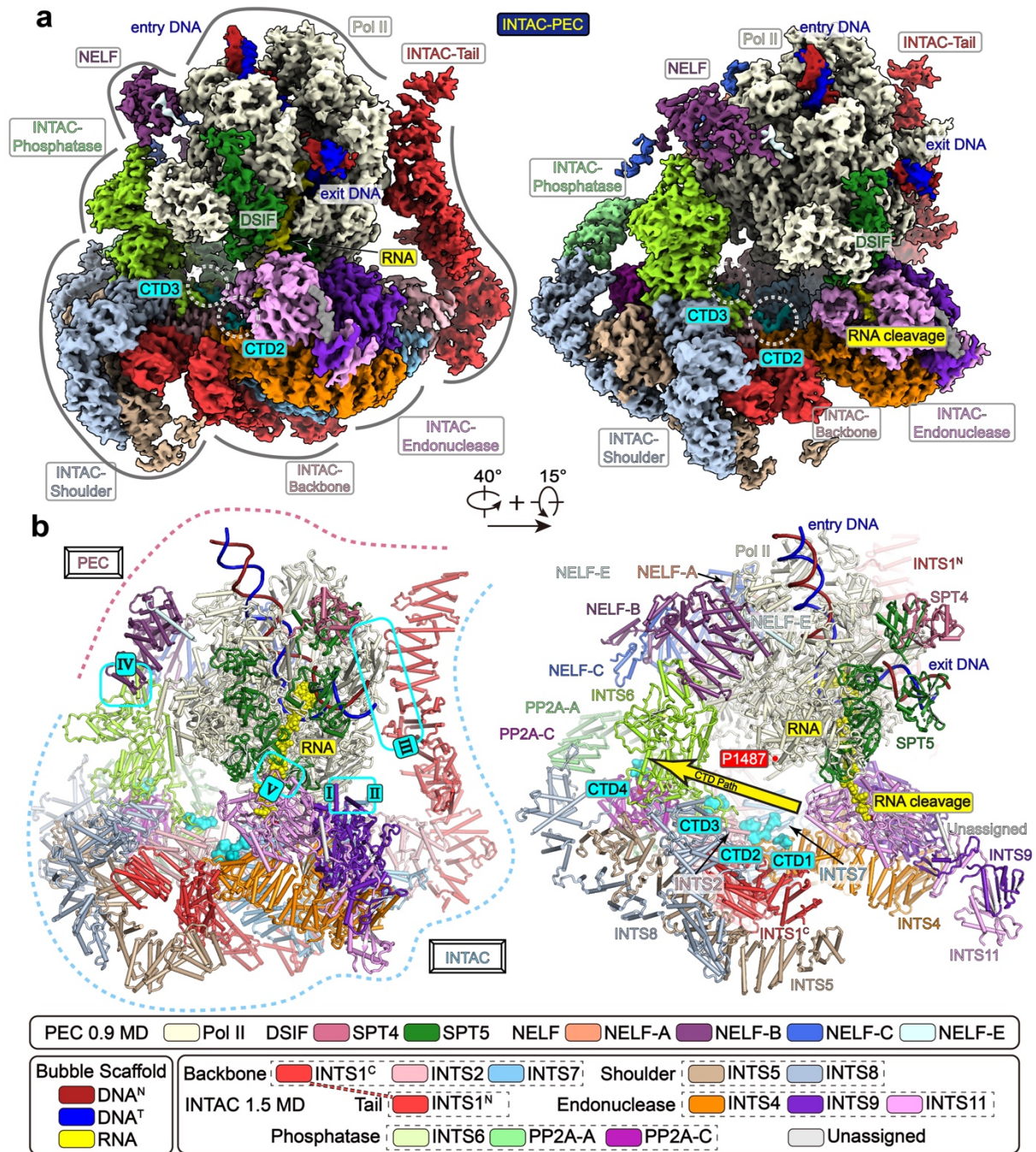
Fig. 1 | Structure of INTAC-PEC complex.

a, b, Composite cryo-EM map (**a**) and structural model (**b**) of INTAC-PEC shown in two different views. Five INTAC-PEC interfaces are indicated and four putative Pol II CTD fragments are shown in surface representation. The same color scheme was used in all of the figures if not otherwise specified. Putative CTD-binding path on INTAC and RNA cleavage site in INTS11 are highlighted.
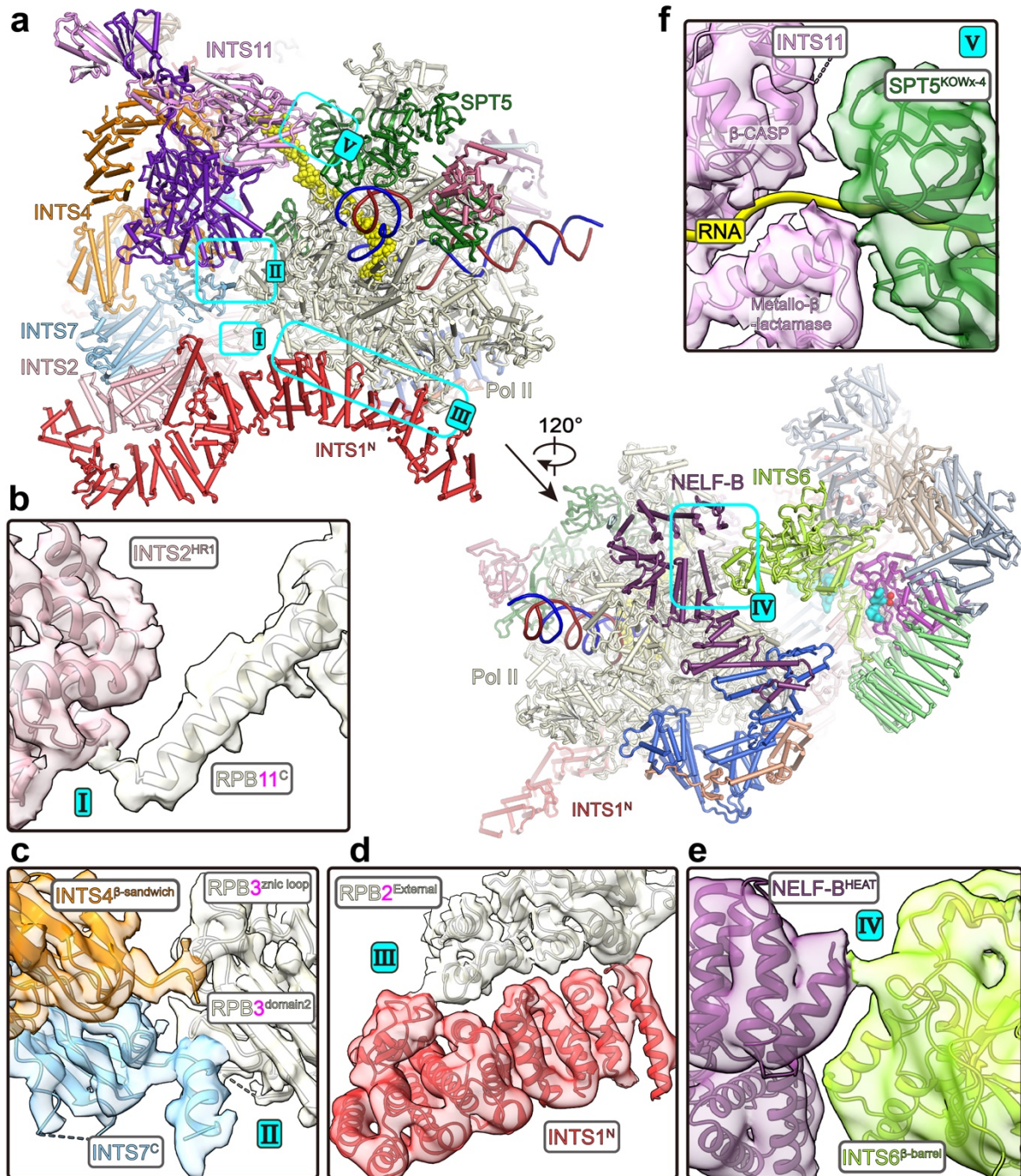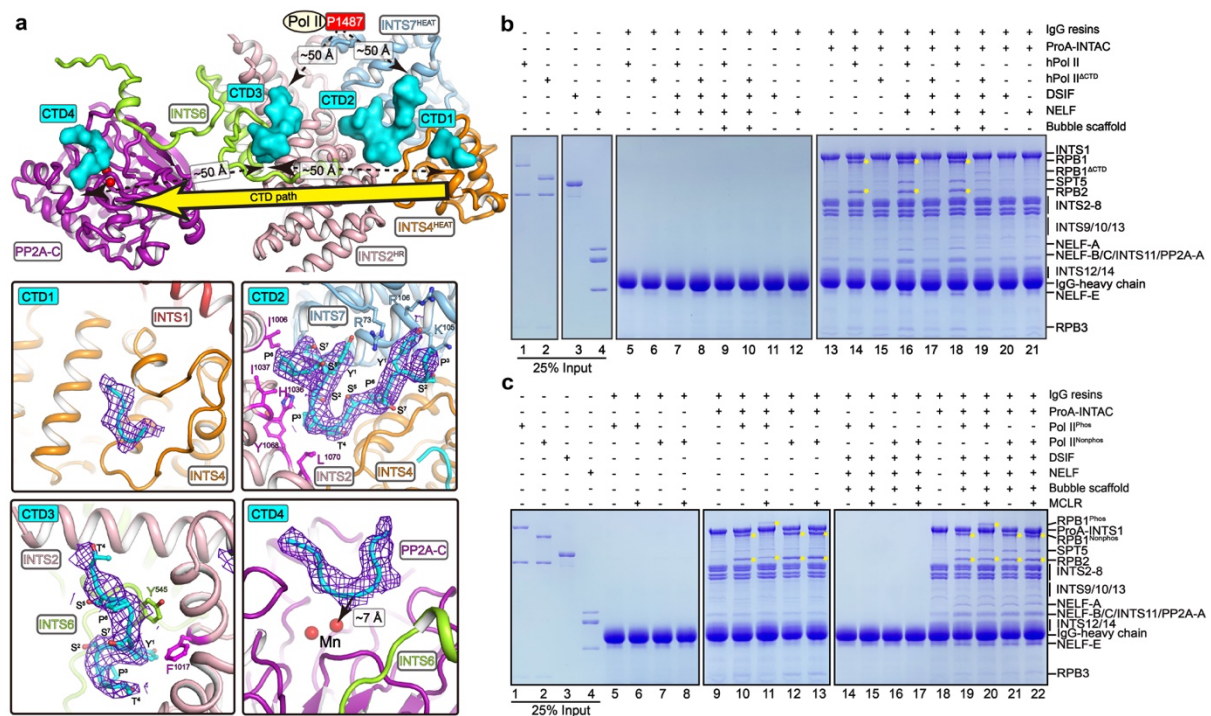
Fig. 2 | Interactions between INTAC and PEC.

a, Overall structure of INTAC-PEC with the five inter-complex contacts highlighted. **b-f,** Close-up views of the interactions with cryo-EM maps shown in transparent surface and structural models shown in cartoon.

419

Fig. 3 | Pol II CTD makes multiple contacts with INTAC and is required for INTAC-Pol II interaction.

a, Close-up view of Pol II CTD-binding path on INTAC. Four putative CTD fragments are shown in surface and non-relevant subunits/domains were omitted for simplicity. The position of residue P1487 (the last modeled residue) of RPB1 is shown to indicate its distance to CTD fragments. The bottom panels show close-up views of the interactions between CTDs and INTAC with CTDs shown in cryo-EM maps (blue meshes) and structural models. Residues involved in interactions of CTD-2 and CTD-3 are shown in sticks. **b, c,** In vitro pulldown assays using purified INTAC and PEC subcomplexes. Protein A (ProA)-tagged INTAC was incubated with indicated subcomplexes and immobilized onto IgG resins. The unbound proteins were washed and immobilized samples were subjected to SDS-PAGE and Coomassie blue staining. Pol II^{phos} represents pig Pol II that underwent in vitro phosphorylation by TFIIH and hPol II and hPol II$^{\Delta CTD}$ represent human Pol II and CTD-truncated human Pol II, respectively. Yellow stars indicate the positions of RPB1 and RPB2, reflecting the binding of Pol II in the reactions.

17
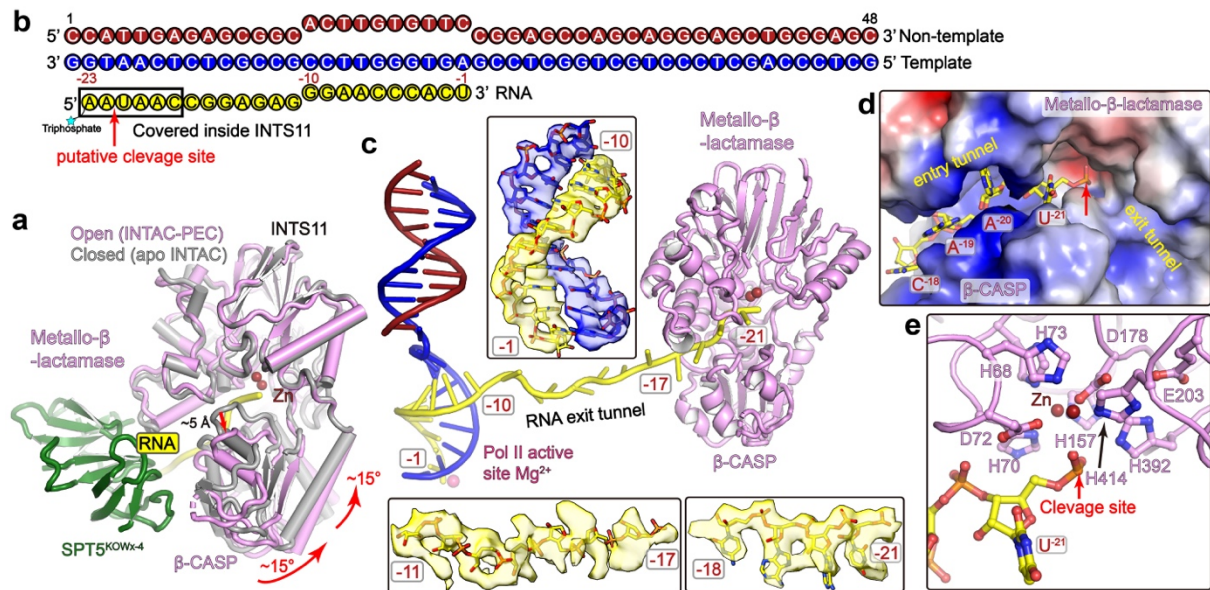
Fig. 4 | RNA is recognized and cleaved by INTS11 in an active conformation.

a, Assembly of INTAC-PEC leads to activation of INTS11. The structures of INTS11 in the apo INTAC (grey) [7] and INTAC-PEC (pink, this study) are superimposed. Rotation of the β-CASP domain and opening of the RNA entry tunnel are indicated with arrows. The movement of INTS11 likely results from binding of PEC and/or RNA. **b-c**, Schematic diagram (b) and structural model (c) of DNA-RNA bubble. Cryo-EM maps of three parts are shown. Assignment of RNA between -11 to -17 was not accurate and the number of nucleotides was proposed based on the length of extended RNA strand. **d, e,** Recognition of RNA by INTS11 within the RNA entry tunnel (d) and above the active site (e). (d) Electrostatic potential surface of INTS11 is shown and RNA is shown in sticks. (e) Organization of the catalytic center and positioning of RNA for cleavage.

Methods

Protein expression and purification

INTAC was overexpressed and purified as previously described [7]. Pol II was isolated from *S. scrofa thymus* and purified following the reported protocol [30,31,40,41]. Four residue substitutions (G882S of RBP2, T75I of RPB3, S140N of RPB3, and S126T of RPB6) exist between *S. scrofa* and *H. sapiens* Pol II.

All the purification steps were performed at 4 °C unless otherwise stated. The two full-length open reading frames (ORFs) of human DSIF subunits (SPT4 and SPT5) were separately subcloned into a modified pCAG vector and SPT4 was tagged with an N-terminal 2 × Protein A. Both plasmids were co-transfected to Expi293 cells using PEI (Polysciences) when the cells reached a density of 2.5×10^6/ml. After being cultured at 37 °C for 60 hours, cells were harvested and lysed in lysis buffer containing 50 mM Na-HEPES pH 7.4, 300 mM NaCl, 0.25% CHAPS, 5 mM MgCl$_2$, 5 mM adenosine triphosphate (ATP), 10% glycerol (v/v), 2 mM dithiothreitol (DTT), 1 mM phenylmethylsulfonyl fluoride (PMSF), 1 μg/ml aprotinin, 1 μg/ml pepstatin, 1 μg/ml leupeptin for 30 min. The lysate was clarified by centrifugation at 16,000 rotations per minute (rpm) for 30 min with JLA-16.250 rotor (Beckman Coulter), and the supernatant was incubated with immunoglobulin G (IgG) resins (Smart-Lifesciences) overnight. The resins were washed with buffer containing 30 mM Na-HEPES pH 7.4, 300 mM NaCl, 0.1% CHAPS, 2 mM MgCl$_2$, 10% glycerol, 2 mM DTT. After on-column cleavage by 3C protease for 4 hours, the immobilized proteins were eluted and further purified by ion exchange chromatography (Mono Q 5/5, GE Healthcare). Peak fractions were assessed by SDS–PAGE followed by Coomassie blue staining. Protein concentration was determined by measuring absorption at 280 nm and using the predicted extinction coefficient for DSIF. Pure fractions were pooled, aliquoted, snap frozen and stored at −80 °C.

NELF was prepared essentially in a similar way as described in DSIF. The four full-length ORFs of human NELF subunits (NELF-A, -B, -D, -E) were separately subcloned into a modified pCAG vector and NELF-E was tagged with an N-terminal 2 × Protein A. The plasmids were co-transfected into Expi293F cells for overexpression. The cells were collected by centrifugation and resuspended in lysis buffer containing 50 mM Na-HEPES pH 7.4, 300 mM NaCl, 0.25% CHAPS, 5 mM MgCl$_2$, 5 mM ATP, 10% glycerol (v/v), 2 mM DTT, 1 mM PMSF, 1 μg/ml aprotinin, 1 μg/ml pepstatin, 1 μg/ml leupeptin. After cell lysis, the lysate was cleared by centrifugation and the supernatant was incubated with IgG resins (Smart-Lifesciences) for 4 hours followed by on-column digestion by 3C protease for 4 hours. The eluate was further purified by ion exchange chromatography (Mono Q 5/5, GE Healthcare). Peak fractions were pooled and protein purity was assessed by SDS–PAGE and Coomassie staining. Pure NELF was concentrated and subjected to in vitro dephosphorylation overnight by Lambda Protein Phosphatase (Lambda PP, Beyotime Biotechnology). The dephosphorylated

483   NELF was applied onto a Superdex200 10/300 GL column (GE Healthcare) in a buffer
484   containing 30 mM K-HEPES pH 7.4, 150 mM KCl, 5% glycerol (v/v), 2 mM DTT. Peak
485   fractions containing NELF were pooled, aliquoted, snap frozen, and stored at −80 °C.
486

Cryo-EM sample preparation

488   DNA oligos were purchased from Generay Biotechnology and RNA oligos were
489   purchased from Bioneer. All oligos were resuspended in RNase-free water (200 µM) and stored
490   at −30 °C. The Pol II elongation complex (EC) was assembled on a bubble scaffold with the
491   following nucleic acid sequences as previously reported with minor modifications [30,31]:
492   template DNA 5′-GCT CCC AGC TCC CTG CTG GCT CCG AGT GGG TTC CGC CGC TCT
493   CAA TGG-3′, non-template DNA 5′-CCA TTG AGA GCG GCA CTT GTG TTC CGG AGC
494   CAG CAG GGA GCT GGG AGC-3′, and RNA 5′-triphosphate-AAU AAC CGG AGA GGG
495   AAC CCA CU-3′. The scaffold contains 10 bp DNA–RNA hybrid, 10-nuclotide bubble, 13
496   nucleotides of exit RNA, 24 nucleotides of entry DNA and 14 nucleotides of exit DNA. To
497   obtain the DNA-RNA hybrid, template DNA and RNA were mixed with a molar ratio of 1:1.3
498   and were annealed by incubating the nucleic acids at 95 °C for 10 min and then decreasing the
499   temperature by 1 °C min^{-1} steps to a final temperature of 4 °C in a thermocycler in a buffer
500   containing 20 mM K-HEPES pH 7.4, 60 mM KCl, 3 mM MgCl$_2$, and 5% (v/v) glycerol. All
501   concentrations refer to the final concentrations used in complex assembly. To assemble EC, the
502   purified *S. scrofa* Pol II (275 pmol) was incubated with twofold molar excess of the DNA-RNA
503   hybrid for 15 min at 30 °C, shaking at 300 rpm, followed by the addition of twofold molar
504   excess of non-template DNA and further incubation for 15 min at 30 °C. The purified DSIF and
505   NELF were added in a twofold molar excess relative to Pol II for the PEC reconstitution. The
506   sample was incubated for 1 hour at 4 °C, followed by the addition of the purified INTAC (250
507   pmol) and incubation for another 2 hours at 4 °C. The resulting sample was subjected to gradient
508   fixation (GraFix) [42]. The glycerol gradient was prepared using light buffer containing 8% (v/v)
509   glycerol, 20 mM K-HEPES pH 7.4, 60 mM KCl, 0.03% CHAPS, 2 3mM MgCl$_2$, mM DTT,
510   and heavy buffer containing 40% (v/v) glycerol, 0.0018% glutaraldehyde (Sigma), 20 mM
511   HEPES pH 7.4, 60 mM KCl, 0.03% CHAPS, 3mM MgCl$_2$, 2 mM DTT. The centrifugation was
512   performed using an SW60 Ti rotor (Beckman Coulter) at 32,000 rpm at 4°C for 14 hours.
513   Subsequently, peak fractions were pooled and the cross-linking reactions were quenched with
514   100 mM Tris-HCl pH7.0. The homogeneity of peak fractions was assessed by negative-stain
515   electron microscopy. Fractions of interest were concentrated to about 1.7 mg/ml and dialyzed
516   overnight against a buffer containing 20 mM K-HEPES pH 7.4, 60 mM KCl, 0.8% glycerol, 1
517   mM tris (2-carboxyethyl) phosphine (TCEP), followed by cryo-EM grid preparation.

518   For negative-stain EM, 5 µl of freshly purified protein sample was applied onto a glow-
519   discharged copper grid supported by a thin layer of carbon film for 1 min before negative
520   staining by 2% (w/v) uranyl formate at room temperature. The negatively stained grid was

20

521 loaded onto a FEI Talos L120C microscope operated at 120 kV, equipped with a Ceta CCD
522 camera.

523   For cryo-EM grid preparation, 4 μl of protein sample (about 0.73 mg/ml) was applied onto
524 a glow-discharged holey carbon grid (Quantifoil Au, R2/2, 300 mesh). After blotting for 3 s,
525 the grid was vitrified by plunging it into liquid ethane using a Vitrobot Mark IV (FEI) operated
526 at 4°C and 100% humidity.

527

528 **IgG pulldown assay**

529   Expi293F cells containing overexpressed INTAC complex were pelleted and lysed as
530 previously described [7]. The supernatant of the cell lysate was incubated with IgG resins for 2
531 hours at 4°C. The INTAC complex was immobilized on the resins by N-terminal 4×Protein A–
532 tagged INTS1. The resins were extensively washed and resuspended in 450 μl of the binding
533 buffer containing 30 mM K-HEPES pH7.4, 100 mM KCl, 0.1% CHAPS, 3 mM $MgCl_2$, 8%
534 glycerol, 2 mM DTT. The purified Pol II or Pol II with deletion of RPB1 CTD (Pol II^{CTD})
535 expressed in Expi293 cells was subjected to removing endogenous RPAP2 by incubating with
536 RPAP2 antibody (Abclonal) on Protein G resins. The resulting Pol II, Pol $II^{\Delta CTD}$, or their the
537 mixture with DSIF and NELF, in the presence or absence of a bubble scaffold was individually
538 incubated with INTAC-immobilized IgG resins for 2 hours at 4°C. The resins were extensively
539 washed with the binding buffer, and the bound proteins were subjected to SDS-PAGE followed
540 by Coomassie blue staining. Other IgG pulldown assays were performed in a similar approach
541 as described above.

542

543 **Cryo-EM data collection and image processing**

544 Cryo-EM data were collected on a Titan Krios electron microscope (FEI) operated at 300 kV
545 at the Cryo-EM platform of Fudan University, equipped with a K2 summit direct detector
546 (Gatan) and a GIF quantum energy filter (Gatan) set to a slit width of 20 eV. Automated data
547 acquisition was carried out with Serial EM software in the superresolution mode [43] at a nominal
548 magnification 130,000×, corresponding to a calibrated pixel size of 1.054 Å, and a defocus
549 range from −1.5 to −2.5 μm. Each image stack was dose fractionated to 32 frames with a total
550 exposure dose of about 50 e−/Å2 and exposure time of 6.72 s. The image stacks were motion-
551 corrected and dose-weighted using MotionCorr2 [44]. The contrast transfer function (CTF)
552 parameters were estimated by CTFFIND-4.1 from non-dose weighted micrographs. About
553 51,000 particles autopicked from 2000 micrographs were subjected into two-dimensional (2D)
554 classification in RELION v3.0 [45] and ab initio reconstruction by cryoSPARC v2 [46]. The 3D
555 initial model was low-passed and used as references for subsequent particle-picking and 3D
556 classification. The following procedures of image processing were performed using RELION
557 for dose-weighted micrographs, 1,237,927 particles were autopicked from 13,956 micrographs
558 for further data processing. After several rounds of   3D classification, 47,736 good particles

559 were selected for further no-alignment 3D classification. Because of the relatively flexible
560 organization between INTAC and PEC, the mask of INTS1-INTS6-INTS9-INTS11-PEC was
561 applied to no-alignment 3D classification to separate the weakly associated INTAC-PEC.
562 Finally, 21,304 particles (stably associated INTAC-PEC) were subjected to 3D-autorefinement,
563 postprocessing, CTF refinement and Bayesian polishing , yielding a reconstruction of INTAC-
564 PEC at 4.47 Å resolution. In order to improve the map quality for model building, focused
565 classification and refinement were used. Afterwards, selected particles were postprocessed,
566 CTF-refined, Bayesian polished and generated reconstructions of the INTAC at 3.92 Å (78,201
567 particles) , INTS2-INTS7-CTD at 3.78 Å (78,201 particles), PP2A-AC at 4.10 Å (70,374
568 particles), INTS9-INTS11-Pol II-DSIF at 3.99 Å (42,152 particles), INTS9-INTS11-RNA at
569 4.10 Å (38,826 particles) and INTS11-RNA at 3.99 Å (38,826 particles). The reported
570 resolutions above are based on the gold-standard Fourier shell correlation (FSC) 0.143 criterion.
571 All the visualization and evaluation of 3D density maps were performed with UCSF Chimera
572 [47] or UCSF ChimeraX [48], and the local resolution variations were calculated using ResMap.
573 The above procedures of data processing are summarized in Extended Data Fig. 2.
574

575 **Model building and structure refinement**
576 The structural model of INTAC-PEC was built according to the 4.47 Å INTAC-PEC cryo-EM
577 map and corresponding focused refined maps. The structures of human INTAC (PDB: 7CUN)
578 and PEC (PDB: 6GML) were used to guide modelling of INTAC-PEC, which were docked into
579 the INTAC-PEC cryo-EM map by rigid body fitting using UCSF Chimera [47] and were manually
580 adjusted using COOT [49]. The models of INTS1, INTS2, INTS4, INTS8, INTS9 and INTS11
581 were further optimized in the guidance of the protein structures predicted by AlphaFold [50]. To
582 build the model of INTS11 (active conformation) and RNA (-18 to -21), the homologous
583 structure of CPSF with nascent RNA (PDB: 6V4X) was used as a reference according to the
584 INTS9-INTS11-RNA map and the model of RNA (-1 to -17) was built using map INTS11-RNA.
585 The structural model of the INTAC-PEC complex was refined against the 4.47 Å overall map
586 in real space with PHENIX [51] and validated through examination of Ramachandran plot
587 statistics, a MolProbity score [52], and a EMRinger score [53]. The statistics of the map
588 reconstruction and model refinement are summarized in Extended Data Table 1. Each focused
589 refined maps were used to create the composite map using UCSF ChimeraX [48]. The composite
590 map was used in Fig. 1a and Supplementary Video 1. Map and model representations in the
591 figures and videos were prepared by PyMOL and UCSF ChimeraX [48].
592